Hindawi
Advances in Materials Science and Engineering
Volume 2018, Article ID 1954573, 8 pages
https://doi.org/10.1155/2018/1954573

Research Article

Real-Time and Quantitative Measurement of Crack-Tip Stress Intensity Factors Using Digital Holographic Interferometry

Haiting Xia,[1,2] **Rongxin Guo**,[1,2] **Feng Yan**,[1,2] **and Heming Cheng**[1]

[1]*Faculty of Civil Engineering and Mechanics, Kunming University of Science and Technology, Kunming, Yunnan 650500, China*
[2]*Key Laboratory of Yunnan Province for Disaster Reduction in Civil Engineering, Kunming University of Science and Technology, Kunming, Yunnan 650500, China*

Correspondence should be addressed to Rongxin Guo; guorx@kmust.edu.cn

Received 8 December 2017; Accepted 22 March 2018; Published 16 May 2018

Academic Editor: Hiroshi Noguchi

Detection of the crack in an object is a critical problem for the health monitoring of a transparent object. The real-time and quantitative measurement of the crack-tip stress intensity factor (SIF) remains an open issue. In this paper, an approach for real-time and quantitative measurement for the SIFs of a Mode I crack is presented based on digital holographic interferometry (DHI). A transmission digital holographic system is established to measure the phase difference of an object wave during loading. The expression to achieve the SIF from the phase difference is formulated. To enhance the accuracy of measurement, calibrated phase unwrapping based on least-squares and iteration and median filtering is applied to retrieve the actual phase from the noisy wrapped one. The SIFs of the Mode I crack in a transparent polymethyl methacrylate (PMMA) specimen are measured by this approach. The results are compared with the theoretical ones to demonstrate the feasibility of the proposed approach.

1. Introduction

Transparent materials are widely used in many engineering applications such as conductive materials [1–3], electrode materials [4–7], thermoelectric materials [8], encapsulation materials [9], and bulletproof materials [10, 11]. The fracture and fatigue problems are critical for many applications of the transparent materials. The crack is the key reason of materials failure. Usually the stress intensity factor (SIF) is the main quantity to evaluate the influence of the crack in the materials in elasticity. In the last decades, many measurement approaches were used to detect the SIF near the crack in transparent materials including photoelasticity [12, 13], coherent gradient sensing (CGS) [14–16], and digital coherent sensing (DGS) [17–19]. However, these approaches need birefringent materials, identification of the fringes, phase shifting, or fabrication of speckles which affect the application and accuracy of the measurement of the SIF.

As a noninvasive and full-field measurement method, digital holographic interferometry (DHI) has been widely used in many measurements including deformation [20–22], contour [23, 24], the field of fluid [25, 26], vibration [27, 28], and microscopy [29, 30]. By applying DHI in the measurement of transparent materials, one can get the stress-optic constant, stress field, and strain field [31, 32]. Especially, DHI can detect the damage and cracks in transparent materials which means it can be used in the health monitoring of a transparent structure and experimental study on the fracture and damage mechanics [33]. Usually, DHI obtains physical quantities through the phase difference of an object wave. As it is obtained through numerical operations based on the arctangent function, the phase is wrapped into the interval $[-\pi, \pi]$ and needed to be unwrapped to retrieve the actual nonwrapped phase [34]. However, because stress near the crack tip is concentrated, the phase fringes are very close which results high speckle noise in the phase maps. The existence of high noise makes phase unwrapping very difficult and even to fail. Spatial filtering can be applied so as to reduce noise before phase unwrapping [35]. However, filtering will smear the phase jumps which will make unwrapping to fail. So, detection of the crack by DHI remains a qualitative analysis and does not realize the quantitative measurement

which limits the application of DHI in the measurement of transparent materials.

In this paper, we aim to realize unwrapping the phase near the crack tip by using the calibrated phase unwrapping method based on least-squares and iterations [36]. Moreover, we present the scheme for the measurement of SIF near the crack tip in a transparent plate by DHI. In addition, the measured results are compared with the theoretical ones to validate the feasibility of the proposed approach. This paper is organized as follows: Section 2 first presents the principles of the proposed approach; Section 3 introduces the experimental scheme of the measurement for K_1 in transparent materials by the proposed approach; in Section 4, the measured results are given and validated by the comparison to the theoretical ones; and some conclusions are given in Section 5 finally.

2. Principles of the Proposed Approach

2.1. Digital Holographic Interferometry. The principle diagram of transmission digital holographic interferometry [31] is shown in Figure 1. The input laser is divided into the object wave and reference wave by a beam splitter. The object wave and reference wave are both expanded and collimated by a spatial filter and a lens, respectively. The transparent object is placed in the collimated object wave and is imaged to the CCD target plane by an equivalent 4f system. Here, the negative lens in the system is used to adjust the field of view of interest. The collimated reference wave is refracted by a beam splitter and interfered with the object wave at the CCD plane. The principle axis of the reference wave forms a certain specified angle with that of the object wave which is normal to the CCD plane so that this system belongs to the image-plane off-axis holography. The CCD camera captures holograms at different loading states. The phase difference related to the stress in the specimen is reconstructed according to the following principles shown in Figure 1.

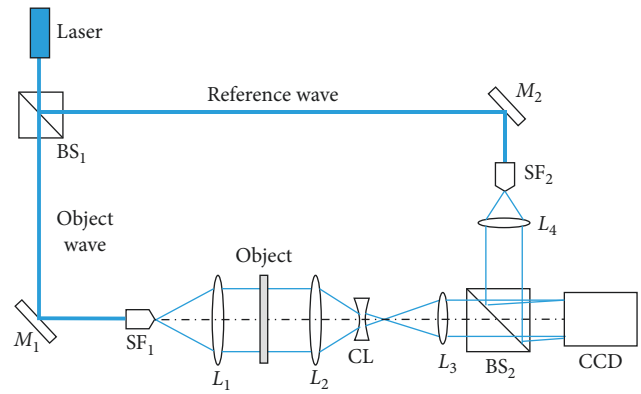

FIGURE 1: Principle diagram of the digital holographic system. BS_1 and BS_2 are the beam splitters; M_1 and M_2 are the mirrors; L_1, L_2, L_3, and L_4 are the positive lenses; CL is the negative lens; SF_1 and SF_2 are the spatial filters.

Establishing x and y coordinates in the CCD plane and z coordinate normal to the plane, the object wave $O(x, y)$ and the reference wave $R(x, y)$ can be expressed as

$$\begin{aligned} O(x, y) &= o(x, y)\exp[jk\varphi(x, y)], \\ R(x, y) &= r(x, y)\exp\left[jk\left(\theta_x x + \theta_y y\right)\right], \end{aligned} \tag{1}$$

where $j = \sqrt{-1}$, $k = 2\pi/\lambda$, λ is the wavelength of the laser, θ_x and θ_y are the angles between z axis and the projection of the reference wave vector on the xz plane and yz plane, respectively.

The hologram captured by the CCD is described as

$$\begin{aligned} I(x, y) = {} & o^2(x, y) + r^2(x, y) + o(x, y)\exp[jk\varphi(x, y)]r(x, y)\exp\left[-jk\left(\theta_x x + \theta_y y\right)\right] \\ & + o(x, y)\exp[-jk\varphi(x, y)]r(x, y)\exp\left[jk\left(\theta_x x + \theta_y y\right)\right]. \end{aligned} \tag{2}$$

Performing Fourier transform on both sides of the above equation, we can get the spectrum of the hologram:

$$\begin{aligned} \mathfrak{F}\{I(x, y)\} = {} & G_0\left(f_x, f_y\right) + G\left(f_x + \frac{\theta_x}{\lambda}, f_y + \frac{\theta_y}{\lambda}\right) \\ & + G^*\left(f_x - \frac{\theta_x}{\lambda}, f_y - \frac{\theta_y}{\lambda}\right). \end{aligned} \tag{3}$$

On the right side of this equation, the first item is the spectrum of the zero-order diffracted wave, the second is the spectrum of the object wave which is modulated by the reference wave and translated to the point $(-\theta_x/\lambda, -\theta_y/\lambda)$ relative to the center of the spectrum plane, and the third is the spectrum of the conjugate object wave. So, by selecting the appropriate angles of θ_x and θ_y, we can separate the spectrum of the object wave $G(f_x, f_y)$ from the other spectrums. A rectangular window filter is used to extract $G(f_x, f_y)$. Then, the inverse Fourier transform of $G(f_x, f_y)$ is carried out to reconstruct the complex modulated object wave $f(x, y)$ as follows:

$$f(x, y) = \mathfrak{F}^{-1}\left\{G\left(f_x, f_y\right)\right\}. \tag{4}$$

The phase difference of object waves at two loading states, due to the specimen's deformation, is expressed as

$$\psi(x, y) = \text{angle}\left[\frac{f_1(x, y)}{f_2(x, y)}\right], \tag{5}$$

where $\psi(x, y)$ is the wrapped phase difference, $f_1(x, y)$ and $f_2(x, y)$ are the complex object waves at different loading states, and angle (.) is the function to calculate the phase angle of a complex value.

2.2. Phase Recovering Approach. In this paper, we use calibrated phase unwrapping algorithm based on the least-squares and iterations (CPULSI) [36] and median filtering to

recover the true phase from the noisy wrapped phase. Here, φ_{ij} represents the true phase and ψ_{ij} ($\in [-\pi, \pi]$, i.e., modulo 2π) represents the wrapped phase at the grid point (i, j) of a phase map. Their relationship can be expressed by the wrapping operator $W(.)$ which is defined as

$$W(\varphi_{ij}) = \psi_{ij} = \varphi_{ij} + 2\pi k_{ij} \quad (i = 0, 1, \ldots, M-1;\ j = 0, 1, \ldots, N-1), \tag{6}$$

where $-\pi \le \psi_{ij} \le \pi$, k_{ij} is an integer, M and N are, respectively, the number of grid points with respect to the i and j indexes. The 1st order spatial wrapped phase derivatives are defined as

$$\begin{aligned}
\Delta_{ij}^{x} &= W(\psi_{(i+1)j} - \psi_{ij}) \quad (i = 0, 1, \ldots, M-2;\ j = 0, 1, \ldots, N-1),\\
\Delta_{ij}^{x} &= 0, \quad \text{otherwise},\\
\Delta_{ij}^{y} &= W(\psi_{i(j+1)} - \psi_{ij}) \quad (i = 0, 1, \ldots, M-1;\ j = 0, 1, \ldots, N-2),\\
\Delta_{ij}^{y} &= 0, \quad \text{otherwise},
\end{aligned} \tag{7}$$

where Δ_{ij}^{x} and Δ_{ij}^{y} are, respectively, the difference with respect to the i and j indexes.

In practice, the presence of noise will generate errors between noisy and noise-free phase derivatives and make unwrapping difficult, even to fail. Here, we proposed a calibration approach in [36] to calibrate the phase derivatives exhibiting large errors:

$$\begin{aligned}
\Delta_{ij}^{x} &= \operatorname{sgn}(\Delta_{ij}^{x})|G_x| \quad \text{if } |\Delta_{ij}^{x}| \ge T_x,\\
\Delta_{ij}^{x} &= \Delta_{ij}^{x}, \quad \text{otherwise},\\
\Delta_{ij}^{y} &= \operatorname{sgn}(\Delta_{ij}^{y})|G_y| \quad \text{if } |\Delta_{ij}^{y}| \ge T_y,\\
\Delta_{ij}^{y} &= \Delta_{ij}^{y}, \quad \text{otherwise},
\end{aligned} \tag{8}$$

where $\operatorname{sgn}(\ldots)$ is the signum function, T_x and T_y are the thresholds, and G_x and G_y are the calibrated phase derivatives. These parameters are defined as ($E[\ldots]$ means the statistical average)

$$\begin{aligned}
T_x &= \sqrt{E\left[(\Delta_{ij}^{x})^2\right] - \left(E[\Delta_{ij}^{x}]\right)^2},\\
T_y &= \sqrt{E\left[(\Delta_{ij}^{y})^2\right] - \left(E[\Delta_{ij}^{y}]\right)^2},\\
G_x &= \frac{1}{MN}\sum_{i=0}^{i=M-1}\sum_{j=0}^{j=N-1}\Delta_{ij}^{x},\\
G_y &= \frac{1}{MN}\sum_{i=0}^{i=M-1}\sum_{j=0}^{j=N-1}\Delta_{ij}^{y}.
\end{aligned} \tag{9}$$

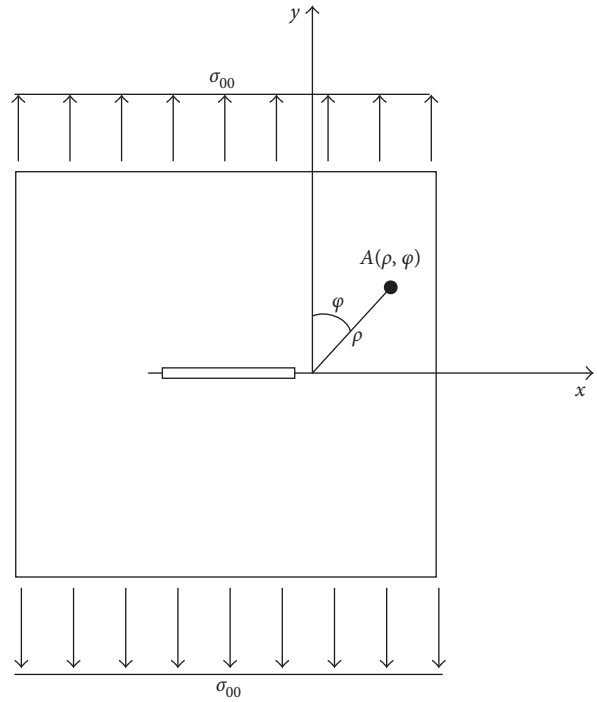

Figure 2: Specimen shape and loading way.

This calibration approach means that the phase derivatives whose values are larger than the standard deviation of phase derivatives are replaced by the average value of phase derivatives.

In the least-squares sense, the optimal solution φ_{ij} can be obtained from the discrete Poisson equation with the Neumann boundary conditions:

$$(\varphi_{(i+1)j} - 2\varphi_{ij} + \varphi_{(i-1)j}) + (\varphi_{i(j+1)} - 2\varphi_{ij} + \varphi_{i(j-1)}) = \rho_{ij}, \tag{10}$$

where

$$\rho_{ij} = (\Delta_{ij}^{x} - \Delta_{(i-1)j}^{x}) + (\Delta_{ij}^{y} - \Delta_{i(j-1)}^{y}). \tag{11}$$

The discrete Poisson equation can be solved by many methods such as fast Fourier transform (FFT), discrete cosine transform (DCT), or the multigrid method. In this algorithm, the DCT method is selected to solve the least-squares phase unwrapping problem.

Theoretically, the solution obtained from (10) is the exact one. However, there exist errors between the unwrapped phase and the true phase due to noise and to the smoothing performance of the least-squares method. In the proposed approach, iterations of unwrapped phase errors are utilized to seek more accurate results [36].

After unwrapping, median filtering is used to reduce the noise in the phase map. Median filtering is one of the most commonly used spatial filtering methods. It uses the median value in the kernel to substitute the value of center of the kernel [37]. So, it is easy to implement and efficient for impulsive noise and speckle noise. In addition, the phase

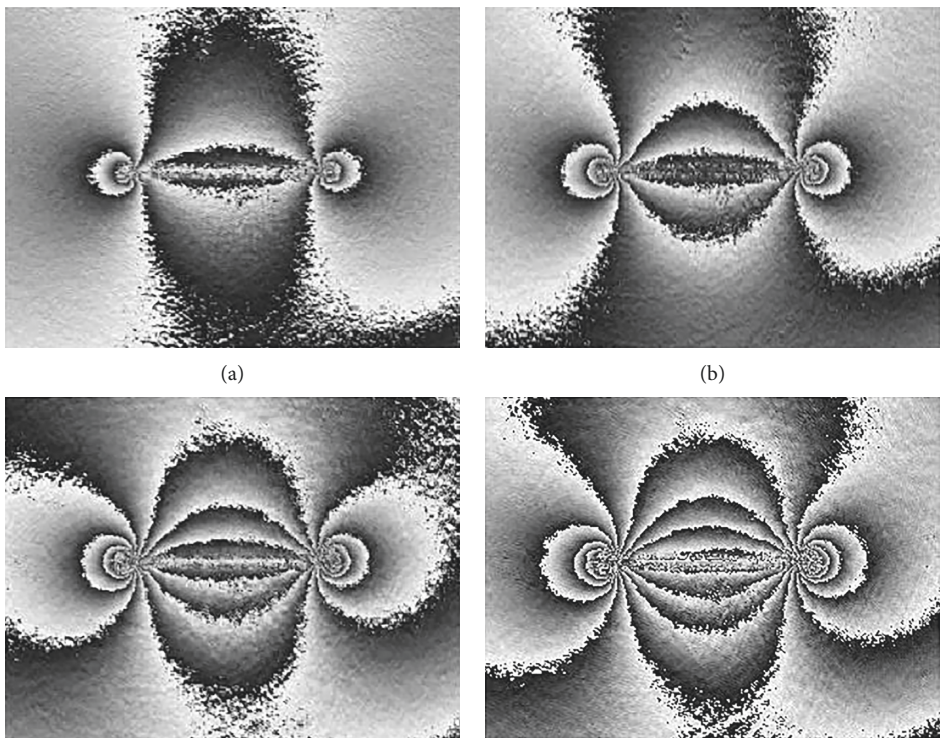

(a) (b) (c) (d)

Figure 3: The wrapped phase of the object wave through the PMMA specimen with a crack. (a) $\sigma_{00} = 1$ MPa, (b) $\sigma_{00} = 1.5$ MPa, (c) $\sigma_{00} = 2$ MPa, and (d) $\sigma_{00} = 2.5$ MPa.

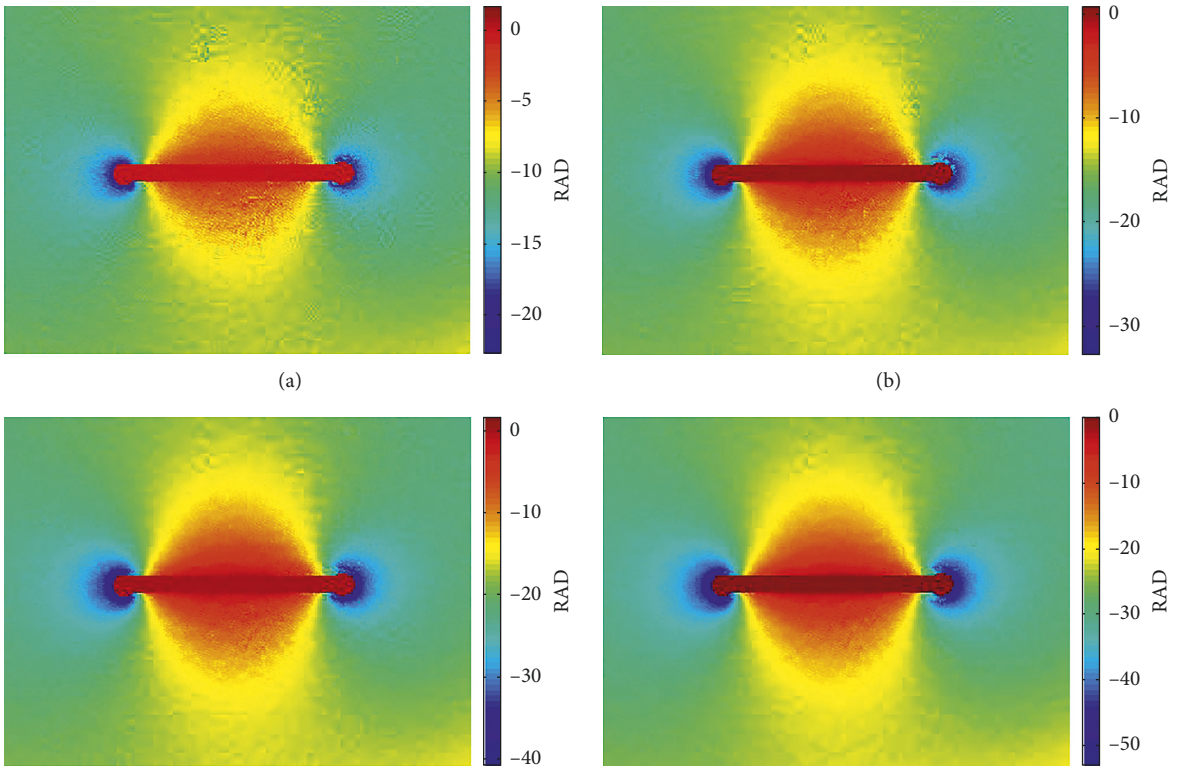

(a) (b) (c) (d)

Figure 4: The unwrapped phase of the object wave through the PMMA specimen with a crack. (a) $\sigma_{00} = 1$ MPa, (b) $\sigma_{00} = 1.5$ MPa, (c) $\sigma_{00} = 2$ MPa, and (d) $\sigma_{00} = 2.5$ MPa.

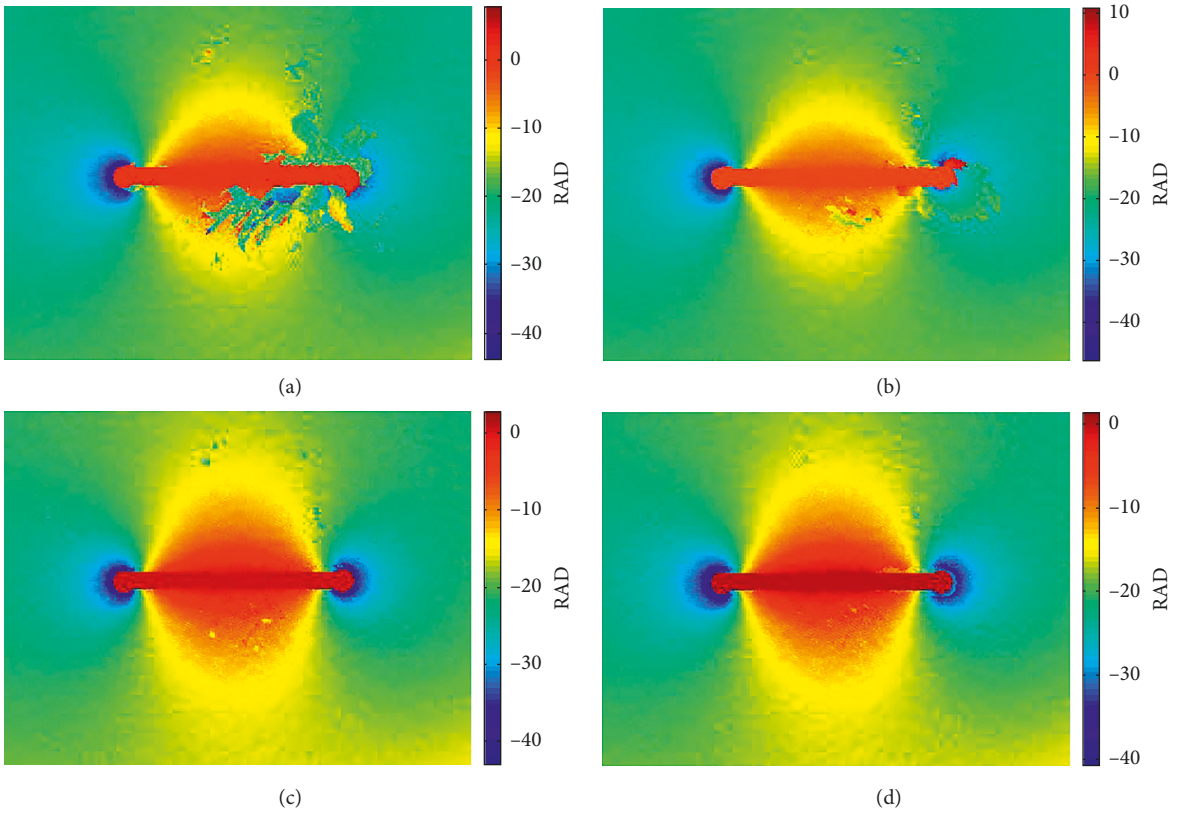

Figure 5: The unwrapped phase of the object wave as $\sigma_{00} = 2$ MPa obtained from (a) Gold, (b) Quality, (c) Flynn, and (d) Lp.

map must be padded out of the frontiers with the length of the kernels symmetrically.

2.3. Calculation of the Stress Intensity Factor. For the uniform transparent plate specimen normal to the object wave principle axis, the relationship between the stress and phase difference of the object wave in plane stress state can be expressed as [31]

$$\left(\sigma_x + \sigma_y\right) = \frac{\lambda}{2\pi hc}\Delta\varphi, \tag{12}$$

where σ_x and σ_y are the normal stresses in the plane, h is the thickness of the plate, c is the stress-optic constant of materials, and $\Delta\varphi$ is the unwrapped denoised phase.

Taking into account the specimen with a Mode I through crack as shown in Figure 2, the stress near the crack tip can be expressed as [38]

$$\sigma_x = \frac{K_{\mathrm{I}}}{\sqrt{2\pi r}}\cos\frac{\theta}{2}\left(1 - \sin\frac{\theta}{2}\sin\frac{3\theta}{2}\right), \tag{13}$$

$$\sigma_y = \frac{K_{\mathrm{I}}}{\sqrt{2\pi r}}\cos\frac{\theta}{2}\left(1 + \sin\frac{\theta}{2}\sin\frac{3\theta}{2}\right), \tag{14}$$

where K_{I} is the stress intensity factor (SIF) of the Mode I crack and r and θ are the polar coordinates relative to the crack tip.

By adding (13) and (14), we can get the equation to calculate K_{I} from the stresses as

$$K_{\mathrm{I}} = \frac{\left(\sigma_x + \sigma_y\right)\sqrt{2\pi r}}{2\cos\left(\theta/2\right)}. \tag{15}$$

So, from (12) and (15), one can calculate the stress sum and SIF near the crack tip.

3. Experiment

In order to validate its feasibility, the proposed approach is used to measure the SIF near the crack tip in a transparent specimen. The specimen is fabricated with polymethyl methacrylate (PMMA). The shape and load of the specimen are shown in Figure 2. The size of the specimen is 400 mm × 100 mm × 4 mm. A through sharp crack is fabricated in the center of the specimen by the fatigue testing machine, and its length is 22 mm. The specimen is subjected to the vertical uniform tensile load σ_{00} increasing from 0 to 3 MPa which has been estimated to ensure linear elasticity. The elastic modulus of PMMA is $E = 3.24$ GPa, and Poisson's ratio is $\nu = 0.35$. The wavelength of the laser is $\lambda = 532$ nm. A 1024 × 768 pixel CCD camera with a pixel size of 6.4 μm is used to record digital holograms.

4. Experimental Results and Validation

4.1. Experimental Results of Phase Difference. By using the image-plane reconstruction algorithm given in Section 2.1, we can obtain the phase difference of any applied load relative to the initial load ($\sigma_{00} = 0$). The wrapped phase

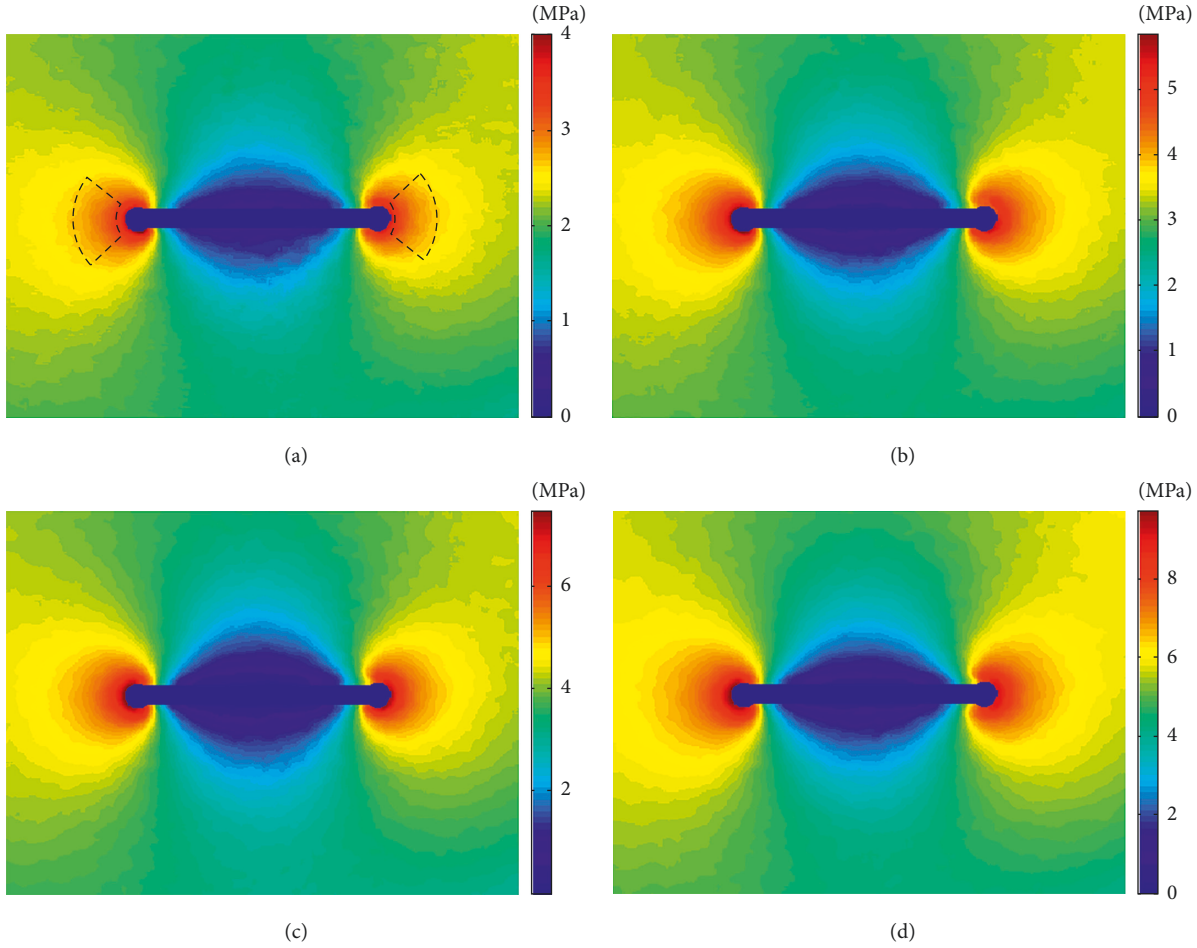

FIGURE 6: The sum of stress $(\sigma_x + \sigma_y)$ in the PMMA specimen with a crack. (a) $\sigma_{00} = 1$ MPa, (b) $\sigma_{00} = 1.5$ MPa, (c) $\sigma_{00} = 2$ MPa, and (d) $\sigma_{00} = 2.5$ MPa.

differences at different load are shown in Figure 3. From these wrapped phase maps, it can be seen that there exists high speckle noise, the fringes near the crack tip are very close, and the phase data inside the crack region is invalid. So, these phase maps are very difficult to unwrap.

In order to unwrap the phase data in Figure 3, we use a mask to shield the crack region; then, CPULSI is used to unwrap the masked phase maps. The unwrapped phase maps are shown in Figure 4, and we can see that all the phase maps are unwrapped successfully.

In order to illustrate the necessity of CPULSI used in this paper, four other different classical phase unwrapping algorithms were selected: Goldstein branch cut algorithm (namely, "Gold"), quality-guided path following algorithm ("Quality"), Flynn's minimum-weight-discontinuity algorithm ("Flynn"), and minimum Lp norm algorithm ("Lp") [34]. Figure 5 shows the unwrapped phase maps of the object wave as $\sigma_{00} = 2$ MPa obtained from these four algorithms. Comparing Figure 4(c), we can see that the unwrapped result from CPULSI is better than those from the other algorithms obviously. In fact, the other algorithms cannot successfully unwrap the phase data in this study because there all exist discontinuities in the maps of Figure 5. So, it is necessary to use CPULSI in this study.

4.2. Calculation of the Stress Field and SIF near the Crack Tip. In order to reduce the noise in the phase maps, median filtering with the kernel size of 21×21 pixels is applied on the unwrapped phase maps. The denoised unwrapped phase is used to calculate stress sum near the crack tip. Figure 6 shows the stress sum as $\sigma_{00} = 1$ MPa, 1.5 MPa, 2 MPa, and 2.5 MPa. From these results, it can be seen that the maximum stress sums exist in the zone near the crack tip and those near the crack plane close to zero which is in accordance with the fracture theory.

According to (15), we can calculate SIFs from stress sums at different loads. Because (13) and (14) only express the stresses infinitely close to the crack tip in the range of linear elastic, and the K-dominate zone must be determined before calculation. Here, we select the dashed sectorial domain in Figure 6(a) which is $1.5\,\text{mm} \le r \le 2.5\,\text{mm}$ and $-45^\circ \le \theta \le 45^\circ$ as the K-dominate zone is referring to some literatures [14, 15, 18, 19]. The average value of the SIFs in the

Table 1: The comparison between the measured values and theoretical values of K_I.

Tensile load (MPa)	Measured K_I (MPa·m$^{0.5}$)	Theoretical K_I (MPa·m$^{0.5}$)	Relative error (%)
1.0	0.193	0.191	1.0
1.5	0.291	0.287	1.4
2.0	0.379	0.383	−1.0
2.5	0.503	0.479	5.0

K-dominate zone is set as the measured value. The measured SIFs at different loads are shown in Table 1.

In order to validate the accuracy of the measurement, the theoretical values of the SIFs are calculated by using the method in [39]. For the crack in Figure 2, K_I can be calculated as

$$K_I = F\sigma_{00}\sqrt{\pi a}, \tag{16}$$

where σ_{00} is the vertical uniform tensile load, a is the half length of the crack, and F is the calibration coefficient for the size of the specimen which can be expressed as

$$F = \left[1 - 0.025\left(\frac{a}{b}\right)^2 + 0.06\left(\frac{a}{b}\right)^4\right]\sqrt{\sec\left(\frac{\pi a}{2b}\right)}, \tag{17}$$

where b is the half width of the specimen. The calculated theoretical values of SIFs at different loads are also shown in Table 1. We can obtain the relative errors by comparing the measured values and theoretical ones. From Table 1, it can be seen that the error of the measured SIF does not exceed 5% which means the results of the proposed approach are accurate.

5. Conclusions

In this paper, we address the real-time and quantitative measurement for the SIFs of the Mode I crack in the transparent plate by DHI. For the phase processing near the crack tip which is affected by the close fringes and high speckle noise, we use phase unwrapping algorithm CPULSI and median filtering to recover the phase maps. The calculation method of K_I from the phase difference is formulated based on linear elastic fracture mechanics. The proposed approach is used to measure K_I of the crack in the PMMA specimen. The measured results are validated in comparison with the theoretical ones. The proposed approach can be used for the real-time and quantitative test of transparent materials.

Conflicts of Interest

The authors declare that they have no conflicts of interest.

Acknowledgments

This work was supported by the Natural Science Foundation of China (11462009 and 11362007).

References

[1] F.-G. Zhao, Y.-T. Kong, Z.-W. Xu, X. Yao, B. Zuo, and W.-S. Li, "High-performance flexible transparent conductive films achieved by cooperation between 1D copper nanowires and 2D graphene materials," *Journal of Materials Chemistry C*, vol. 5, pp. 5509–5516, 2017.

[2] B. Yang, C. Yao, Y. Yu, Z. Li, and X. Wang, "Nature degradable, flexible, and transparent conductive substrates from green and earth-abundant materials," *Scientific Reports*, vol. 7, no. 1, 2017.

[3] Q. Tang, H. Shen, H. Yao, Y. Jiang, C. Zheng, and K. Gao, "Preparation of silver nanowire/AZO composite film as a transparent conductive material," *Ceramics International*, vol. 43, no. 1, pp. 1106–1113, 2017.

[4] M. Wu, D. Sun, C. Tan, X. Tian, and Y. Huang, "Al-doped ZnO monolayer as a promising transparent electrode material: a first-principles study," *Materials*, vol. 10, no. 4, p. 359, 2017.

[5] G. Wroblewski, B. Swatowska, W. Powroznik, M. Jakubowska, and T. Stapinski, "Structural and optical properties of spray coated carbon hybrid materials applied to transparent and flexible electrodes," *Journal of Nanomaterials*, vol. 2017, Article ID 3424672, 7 pages, 2017.

[6] M. D. S. L. Wimalananda, J.-K. Kim, and J.-M. Lee, "Toward the ultra-transparent electrode by using patterned silver nanowire and graphene layered material," *Carbon*, vol. 125, pp. 9–19, 2017.

[7] T. Q. Trung and N.-E. Lee, "Materials and devices for transparent stretchable electronics," *Journal of Materials Chemistry C*, vol. 5, no. 9, pp. 2202–2222, 2017.

[8] C. Yang, D. Souchay, M. Kneiβ et al., "Transparent flexible thermoelectric material based on non-toxic earth-abundant p-type copper iodide thin film," *Nature Communications*, vol. 8, p. 16076, 2017.

[9] D. J. Kang, G. U. Park, H. Y. Park, and H.-G. Im, "A robust transparent encapsulation material: Silica nanoparticle-embedded epoxy hybrid nanocomposite," *Composites Science and Technology*, vol. 144, pp. 107–113, 2017.

[10] T. Benitez, S. Y. Gómez, A. P. N. de Oliveira, N. Travitzky, and D. Hotza, "Transparent ceramic and glass-ceramic materials for armor applications," *Ceramics International*, vol. 43, no. 16, pp. 13031–13046, 2017.

[11] G.-I. Shim, S.-H. Kim, D.-L. Ahn et al., "Experimental and numerical evaluation of transparent bulletproof material for enhanced impact-energy absorption using strengthened glass/polymer composite," *Composites Part B*, vol. 97, pp. 150–161, 2016.

[12] S. Khaleghian, A. Emami, M. Tehrani, and N. Soltani, "Analysis of effective parameters for stress intensity factors in the contact problem between an asymmetric wedge and a half-plane using an experimental method of photoelasticity," *Materials and Design*, vol. 43, pp. 447–453, 2013.

[13] M. D. Ellingsen and S. K. Khanna, "Experimental investigation of static interfacial fracture in orthotropic polymer composite bimaterials using photoelasticity," *Journal of Engineering Materials and Technology*, vol. 132, no. 2, p. 021007, 2010.

[14] K. Ma and H. Xie, "Mixed-mode fracture investigation of PMMA with initial single/double crack(s) interference using phase-shifted coherent gradient sensing method," *Polymer Testing*, vol. 59, pp. 296–307, 2017.

[15] K. Ma and H. Xie, "A novel phase shifting technique of coherent gradient sensing method for measuring crack-tip

K-dominance," *Experimental Mechanics*, vol. 57, no. 8, pp. 1239–1248, 2017.

[16] X. F. Yao, H. Y. Yeh, and W. Xu, "Fracture investigation at V-notch tip using coherent gradient sensing (CGS)," *International Journal of Solids and Structures*, vol. 43, no. 5, pp. 1189–1200, 2006.

[17] B. M. Sundaram and H. V. Tippur, "Dynamic mixed-mode fracture behaviors of PMMA and polycarbonate," *Engineering Fracture Mechanics*, vol. 176, pp. 186–212, 2017.

[18] B. M. Sundaram and H. V. Tippur, "Dynamics of crack penetration vs. branching at a weak interface: an experimental study," *Journal of the Mechanics and Physics of Solids*, vol. 96, pp. 312–332, 2016.

[19] C. Periasamy and H. V. Tippur, "Measurement of crack-tip and punch-tip transient deformations and stress intensity factors using digital gradient sensing technique," *Engineering Fracture Mechanics*, vol. 98, pp. 185–199, 2013.

[20] S. Montrésor, P. Picart, O. Sakharuk, and L. Muravsky, "Error analysis for noise reduction in 3D deformation measurement with digital color holography," *Journal of the Optical Society of America B*, vol. 34, pp. B9–B15, 2017.

[21] D. Khodadad, A. K. Singh, G. Pedrini, and M. Sjödahl, "Full-field 3D deformation measurement: comparison between speckle phase and displacement evaluation," *Applied Optics*, vol. 55, no. 27, pp. 7735–7743, 2016.

[22] G. N. Oliveira, D. M. C. Rodrigues, L. C. S. Nunes, and P. A. M. dos Santos, "Digital Fourier transform holography applied to investigate mechanical deformation in polymers," *Optics and Lasers in Engineering*, vol. 50, no. 12, pp. 1798–1803, 2012.

[23] V. Lédl, P. Psota, F. Kaván, O. Matoušek, and P. Mokrý, "Surface topography measurement by frequency sweeping digital holography," *Applied Optics*, vol. 56, pp. 7808–7814, 2017.

[24] M. Dekiff, P. Berssenbrügge, B. Kemper, C. Denz, and D. Dirksen, "Simultaneous acquisition of 3D shape and deformation by combination of interferometric and correlation-based laser speckle metrology," *Biomedical Optics Express*, vol. 6, pp. 4825–4840, 2015.

[25] C. Hesseling, T. Homeyer, J. Peinke, and G. Gülker, "Particle depth position detection by 2D correlation in digital in-line holography," *Optics Letters*, vol. 41, no. 21, pp. 4947–4950, 2016.

[26] J.-M. Desse, P. Picart, and F. Olchewsky, "Quantitative phase imaging in flows with high resolution holographic diffraction grating," *Optics Express*, vol. 23, no. 18, pp. 23726–23737, 2015.

[27] K. A. Stetson, "Effect of changing speckles in digital holography on measurements of static and vibratory displacements," *Applied Optics*, vol. 55, no. 16, pp. 4485–4489, 2016.

[28] J. Poittevin, P. Picart, F. Gautier, and C. Pezerat, "Quality assessment of combined quantization-shot-noise-induced decorrelation noise in high-speed digital holographic metrology," *Optics Express*, vol. 23, no. 24, pp. 30917–30932, 2015.

[29] W. J. Eldridge, A. Sheinfeld, M. T. Rinehart, and A. Wax, "Imaging deformation of adherent cells due to shear stress using quantitative phase imaging," *Optics Letters*, vol. 41, no. 2, pp. 352–355, 2016.

[30] M. Malek, H. Khelfa, P. Picart, D. Mounier, and C. Poilâne, "Microtomography imaging of an isolated plant fiber: a digital holographic approach," *Applied Optics*, vol. 55, no. 3, pp. A111–A121, 2016.

[31] H. Xia, R. Guo, F. Yan et al., "Simultaneous measurement of stress-optic constant and stress field of transparent plate by digital holographic interferometry," *Optik-International Journal for Light and Electron Optics*, vol. 127, no. 24, pp. 11974–11981, 2016.

[32] H. Xia, R. Guo, Z. Fan, H. Cheng, and B. Yang, "Non-invasive mechanical measurement for transparent objects by digital holographic interferometry based on iterative least-squares phase unwrapping," *Experimental Mechanics*, vol. 52, no. 4, pp. 439–445, 2012.

[33] R. Guo, H. Xia, Z. Fan, B. Yang, and T. He, "Research on the interaction of collective cracks with digital holography," *Laser Journal*, vol. 30, pp. 38-39, 2009, in Chinese.

[34] D. C. Ghiglia and M. D. Pritt, *Two-Dimensional Phase Unwrapping: Theory, Algorithms, and Software*, Wiley, Hoboken, NJ, USA, 1998.

[35] S. Montresor and P. Picart, "Quantitative appraisal for noise reduction in digital holographic phase imaging," *Optics Express*, vol. 24, no. 13, pp. 14322–14343, 2016.

[36] H. Xia, S. Montresor, R. Guo et al., "Phase calibration unwrapping algorithm for phase data corrupted by strong decorrelation speckle noise," *Optics Express*, vol. 24, no. 25, pp. 28713–28730, 2016.

[37] S. A. Villar, S. Torcida, and G. G. Acosta, "Median filtering: a new insight," *Journal of Mathematical Imaging and Vision*, vol. 58, no. 1, pp. 130–146, 2017.

[38] Z. N. Li, *Applied Fracture Mechanics*, Behang University Press, Beijing, China, 2012, in Chinese.

[39] Chinese Aeronautical Establishment, *Handbook of Stress-Intensity Factors-Revised Edition*, Science Press, Beijing, China, 1993, in Chinese.